



# Volume-Averaged Electrochemical Performance Modeling of 3D Interpenetrating Battery Electrode Architectures

Bradley L. Trembacki,<sup>1,\*</sup> Ajay Vadakkepat,<sup>2</sup> Scott A. Roberts,<sup>1,\*</sup> and Jayathi Y. Murthy<sup>3</sup>

<sup>1</sup>Sandia National Laboratories, Albuquerque, New Mexico 87185, USA

<sup>2</sup>Qualcomm Inc., San Diego, California, USA

<sup>3</sup>The University of California Los Angeles, Los Angeles, California 90024, USA

Recent advancements in micro-scale additive manufacturing techniques have created opportunities for design of novel electrode geometries that improve battery performance by deviating from the traditional layered battery design. These 3D batteries typically exhibit interpenetrating anode and cathode materials throughout the design space, but the existing well-established porous electrode theory models assume only one type of electrode is present in each battery layer. We therefore develop and demonstrate a multi-electrode volume-averaged electrochemical transport model to simulate transient discharge performance of these new interpenetrating electrode architectures. We implement the new reduced-order model in the PETSc framework and assess its accuracy by comparing predictions to corresponding mesoscale-resolved simulations that are orders of magnitude more computationally-intensive. For simple electrode designs such as alternating plates or cylinders, the volume-averaged model predicts performance within ~2% for electrode feature sizes comparable to traditional particle sizes (5-10 μm) at discharge rates up to 3C. When considering more complex geometries such as minimal surface designs (i.e. gyroid, Schwarz P), we show that using calibrated characteristic diffusion lengths for each design results in errors below 3% for discharge rates up to 3C. These comparisons verify that this novel model has made reliable cell-scale simulations of interpenetrating electrode designs possible.

© The Author(s) 2019. Published by ECS. This is an open access article distributed under the terms of the Creative Commons Attribution Non-Commercial No Derivatives 4.0 License (CC BY-NC-ND, <http://creativecommons.org/licenses/by-nc-nd/4.0/>), which permits non-commercial reuse, distribution, and reproduction in any medium, provided the original work is not changed in any way and is properly cited. For permission for commercial reuse, please email: [oa@electrochem.org](mailto:oa@electrochem.org). [DOI: 10.1149/2.0072001JES]



Manuscript submitted May 29, 2019; revised manuscript received August 21, 2019. Published September 23, 2019. *This paper is part of the JES Focus Issue on Mathematical Modeling of Electrochemical Systems at Multiple Scales in Honor of Richard Alkire.*

Increasing interest in green alternatives to energy transport and storage has led to significant growth in lithium-ion battery research over the past several decades.<sup>1,2</sup> Though well-developed for portable electronics applications, there are numerous challenges to be overcome for the use of lithium-ion batteries in demanding applications like electric vehicles or grid storage.<sup>3-7</sup> Modeling and simulation of these battery systems will play a critical role in their effective and safe commercialization for such high energy/power density applications.<sup>8-10</sup>

A typical lithium-ion battery consists of alternating layers of anode and cathode material with an insulating separator between them. On the micro-scale, the layers consist of a porous composite anode and cathode filled with a liquid electrolyte and separated by a porous separator.<sup>11</sup> Both the anode and cathode are composed of spatially dispersed active particles of lithium insertion compounds (LiCoO<sub>2</sub>, LiNi<sub>x</sub>Mn<sub>y</sub>Co<sub>1-x-y</sub>O<sub>2</sub>, LiFePO<sub>4</sub>, graphite, etc.), polymeric binder, and conductive additives, forming porous particle beds.<sup>12</sup> The electrolyte resides in the pores, wetting the active particle bed and providing a high electrode/electrolyte interfacial surface area for electrochemical reactions to occur.<sup>13</sup> The anode-separator-cathode stack percolated with electrolyte is sandwiched between two current collectors, depicted in Figure 1. This architecture facilitates the shuttling of lithium ions between anode and cathode through the electrolyte while forcing the flow of electrons through the external circuit, thus delivering power. Experimentalists are continuously trying to improve the performance of batteries by varying the shapes and sizes of the active particles, material volume fractions, calendaring process, etc.<sup>14-18</sup>

The manufacturing process of a traditional battery consists of depositing large areas of an anode particle bed slurry, porous electrolyte separator, and cathode particle bed slurry.<sup>19</sup> This layer-by-layer approach generates a battery design where all ions must traverse a significant distance to move between electrodes, which has led to a growing interest in developing electrode configurations that differ significantly from particle beds. Electrode configurations that have the potential to improve battery performance using interpenetrating configurations that shorten ion path lengths have been proposed.<sup>20</sup> There has been

recent interest in using cutting edge micro-scale additive manufacturing techniques to print active electrode materials and fabricate microbatteries that were previously only theoretical.<sup>21-23</sup> Alternating-plate 3D interpenetrating lithium-ion batteries (depicted in Figure 2)

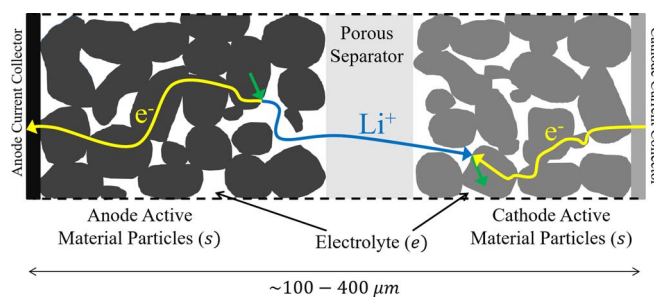


**Figure 1.** Typical layered particle bed battery geometry. Representative discharge transport pathways are depicted for electrons (yellow), intercalated lithium (green), and lithium ions in the electrolyte (blue).

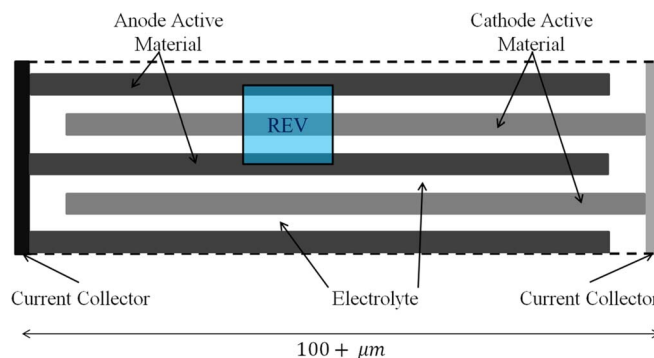


**Figure 2.** Representation of an alternating plate interpenetrating 3D battery geometry with an example representative elemental volume (REV) highlighted in blue.

\*Electrochemical Society Member.

<sup>2</sup>E-mail: [btremba@sandia.gov](mailto:btremba@sandia.gov)

with resolutions as low as 10  $\mu\text{m}$  have shown promise in improving electrochemical performance.<sup>24,25</sup> Microbatteries with inverse opal nanostructures have demonstrated significant increases in power density over other microbatteries and supercapacitors.<sup>21</sup> Others have used various etching and lithography fabrication techniques to develop 3D batteries using arrays of electrode cylinders.<sup>26–29</sup>

The spatial concentration of the lithium ions and electric potential gradients govern the transport of species and charge throughout the battery. Models including governing equations for species and charge transport as well as charge transfer kinetics at the electrode-electrolyte interface are well-established.<sup>13</sup> Solutions of the species and charge transport equations with appropriate boundary and interfacial conditions yield the spatial and temporal distribution of concentration and electric potential fields in the different phases, information that is difficult or impossible to obtain experimentally. Applying these governing equations to fully resolved mesoscale electrode geometries, explicitly partitioned into various constituent phases, can be termed as mesoscale modeling and has grown in recent years due to advancements in both micro-scale imaging techniques and computational resources.<sup>30–36</sup>

While mesoscale simulations can offer significant insight into transport phenomena within a composite electrode, volume-averaged models (also termed continuum scale modeling or porous electrode theory) have the ability to simulate electrochemical behavior of batteries on a full cell scale.<sup>13,37,38–42</sup> Volume averaging involves homogenization of the various phases of the porous electrode, eliminating the need to resolve the electrode microstructure.<sup>43</sup> The governing equations are averaged over a representative elementary volume (REV) that contains both electrolyte and electrode phases. Such an REV is large compared to the size of a typical particle, but small compared to the overall battery cell size. Instead of the intrinsic properties of the various constituents, these models employ effective transport properties that are analytically derived based on various geometric simplifications.<sup>44</sup> Volume-averaging a cell sandwich along with assumptions of homogeneous electrodes can effectively reduce the transport equations to be one-dimensional, since the only direction of transport is between the current collectors on either end of the battery. This reduction in dimensionality makes full battery simulations possible in a reasonable timeframe. These 1D models are most often extended to be pseudo-2D, where the radially symmetric 1D diffusive transport of lithium within a spherical active material particle is evaluated as a sub-grid model at each point in the 1D electrode domain.<sup>38,45</sup> Rather than numerically solve the radial transport, several alternative approaches to capturing solid diffusion within a volume-averaged simulation, such as polynomial approximations and other sub-grid methods, have been published,<sup>46,47</sup> but we focus solely on the diffusion length method throughout this study.<sup>48</sup>

Published work on volume-averaged battery simulation assumes that there are three distinct regions in the battery: an anode region, a separator region, and a cathode region. This is due to the inherently layered design of traditional particle bed batteries, as shown in Figure 1, and is not applicable for interpenetrating electrode geometries where an REV contains both anode and cathode material as in Figure 2. Mesoscale models and simulations of various 3D interpenetrating batteries have been published,<sup>49,50</sup> including our previous work that developed a mesoscale electrochemical-transport simulation capability to study performance of novel 3D interpenetrating battery designs;<sup>33</sup> however, reduced-order models have not been developed.

As a natural complement to the 3D battery mesoscale modeling in the literature, we develop and evaluate, for the first time, a volume-averaged porous electrode theory formulation for interpenetrating 3D battery geometries. It is necessary to average all three material domains (anode, cathode, and electrolyte) together to accurately represent interpenetrating structures. This approach deviates from the traditional two-material volume-averaged formulations that correspond to particle-bed electrode geometries. In this paper, we present this new volume-averaged electrochemical model and use the finite volume method to discretize and implement it in the PETSc software framework, enabling battery-level simulations of 3D interpenetrating battery electrode architectures. Comparisons with mesoscale discharge results

of up to 12C are presented and discussed to assess the accuracy of the model and to provide appropriate characteristic diffusion lengths for unique minimal-surface electrode geometries.

## Governing Equations

Here we present the equations that govern the electrochemical physics relevant to a battery discharge simulation, including conservation of species and charge as well as Butler-Volmer interface kinetics. A more detailed discussion of these equations has been previously published.<sup>33</sup> Figure 1 shows a typical porous electrode cell sandwich consisting of microscale particles of both anode and cathode separated by a separator. As depicted with colored arrows in the figure, during discharge, lithium stored in an anode particle diffuses toward the particle surface where it undergoes a chemical reaction, splitting into a lithium ion and an electron. The lithium ion then traverses the electrolyte to the cathode, while the electron travels toward the anode current collector through the electrically conductive solid phase network, then through the external circuit (providing power), and finally through the cathode current collector and into the cathode active material. At the cathode/electrolyte surface, a lithium ion from the electrolyte joins with a free electron, creating lithium that is free to diffuse through the cathode active material. The opposite pathways and reactions occur during a charge, but power must be provided to force the battery into a higher potential (charged) state by moving lithium from the cathode to the anode. Throughout this study, we assume that the separator region is pure electrolyte and also neglect resolving composite electrode additives such as binder and carbon, choosing to instead incorporate the conductive effects into the intrinsic active material properties, an approach well-established in the field.<sup>45</sup>

**Mesoscale electrochemistry and transport.**—The physical processes involved in lithium-ion electrochemical battery simulations are charge and mass transport. Butler-Volmer kinetics are assumed to govern both charge and mass transport across the electrode-electrolyte interface. In the equations below, subscripts  $e$  and  $s$  represent the electrolyte phase and solid electrode phase (anode/cathode), respectively. The variables of interest are  $c$ , representing lithium concentration, and  $\phi$ , representing electric potential. These equations are applied to both the anode and the cathode.

Charge is conserved within each phase, since it is assumed that no electrochemical reactions are taking place except at the electrode/electrolyte interface.<sup>8,43,48</sup> This leads to the current density conservation equation

$$\nabla \cdot (i_k) = 0 \quad [1]$$

where  $i$  represents current density and subscript  $k$  denotes phase  $s$  or  $e$ . For each phase, applying Ohm's law to (1) and including a non-dilute or concentrated solution modification<sup>38</sup> for the electrolyte equation results in

$$\nabla \cdot (-\sigma_s \nabla \phi_s) = 0 \quad [2]$$

$$\nabla \cdot (-\kappa_e \nabla \phi_e) + \nabla \cdot (-\kappa_D \nabla \ln c_e) = 0 \quad [3]$$

where  $\sigma_s$  is electrode electrical conductivity and  $\kappa_e$  is electrolyte ionic conductivity.<sup>51</sup> The diffusional conductivity,  $\kappa_D$  is expressed as

$$\kappa_D = \frac{2RT\kappa_e}{F} (t_+ - 1) \left( 1 + \frac{\partial \ln f}{\partial \ln c_e} \right) \quad [4]$$

where  $R$  is the universal gas constant,  $T$  is temperature,  $F$  is Faraday's constant, and  $t_+$  is the lithium ion transference number. For this work, temperature, lithium ion transference number, and the activity coefficient  $f$  are assumed to be constant.<sup>40</sup>

In a similar manner, the lithium species is conserved within each phase,<sup>8</sup> yielding

$$\frac{\partial (c_s)}{\partial t} + \nabla \cdot (-D_s \nabla c_s) = 0 \quad [5]$$

$$\frac{\partial (c_e)}{\partial t} + \nabla \cdot (-D_e \nabla c_e) = 0 \quad [6]$$

Intrinsic mass diffusivities ( $D_s, D_e$ ) and conductivities ( $\sigma_s, \kappa_e$ ) are assumed to be constant values.

The boundary conditions for scalar transport Equations 2, 3, 5 and 6 are shown on a simplified 2D battery cell image in Figure 3. In the figure, lines AB and CD represent current collector boundaries, where current enters and leaves the domain. Species transport boundary conditions at the current collector boundaries are described by

$$\mathbf{n} \cdot \nabla c_s = 0 \text{ at } x = 0, W \quad [7]$$

and

$$\mathbf{n} \cdot \nabla c_e = 0 \text{ at } x = 0, W \quad [8]$$

where  $\mathbf{n}$  denotes the outward normal vector on each respective boundary. Here,  $x$  represents the coordinate direction along the battery width, and  $W$  is the battery width, or distance between boundaries AB and CD. The current density condition applied at the CD boundary to the cathode material is

$$\mathbf{n} \cdot (-\sigma_s \nabla \phi_s) = \frac{A_{BB}}{A_{CB}} I_{app} \text{ at } x = W \quad [9]$$

where  $I_{app}$  is the specified applied areal current density leaving the battery boundary during the battery discharge,  $A_{BB}$  is total battery boundary area, and  $A_{CB}$  is total cathode boundary area, which is always equal to or less than  $A_{BB}$ .

In order to set the level of cell voltage and yield a unique solution, a Dirichlet boundary condition of an arbitrary value of 0 volts is set for the anode material at the AB boundary, yielding

$$\phi_s = 0 \text{ at } x = 0 \quad [10]$$

Electrical current can only flow out of the computational domain through the current collectors, i.e. only through the electrode material current collector boundary. This yields a zero current condition of

$$\mathbf{n} \cdot (\kappa_e \nabla \phi_e + \kappa_D \nabla \ln c_e) = 0 \text{ at } x = 0, W \quad [11]$$

on the electrolyte region of the current collector boundaries AB and CD.

Lines AC and BD represent cuts through the battery cell where geometrically appropriate or necessitated by computational resources. Although the image is 2D, similar cuts are made in the third dimension as well (into and out of the page) for 3D simulations. Here we apply a periodic condition, where opposing boundaries are assumed to be adjacent to one another.<sup>40</sup>

A widely accepted approach used to model the electrochemical charge transport across electrode/electrolyte interfaces is the use of Butler-Volmer kinetics relations.<sup>51</sup> The Butler-Volmer kinetic equation governs the interface current density,  $j$ , as

$$j = i_0 \left[ \exp\left(\frac{\alpha_a F}{RT} \eta\right) - \exp\left(-\frac{\alpha_c F}{RT} \eta\right) \right] \quad [12]$$

where  $i_0$  is the exchange current density and  $\alpha_a$  and  $\alpha_c$  are anode and cathode constants, taken to be 0.5. The exchange current density is

represented by

$$i_0 = kF(c_e)^{\alpha_a} (c_{s,max} - c_s)^{\alpha_a} (c_s)^{\alpha_c} \quad [13]$$

where  $k$  is the Butler-Volmer reaction rate constant and  $c_{s,max}$  is the maximum allowable intercalated lithium concentration for the given electrode material.<sup>40</sup> The local overpotential at the interface,  $\eta$ , is defined as

$$\eta = \phi_s - \phi_e - U(\theta) \quad [14]$$

where the  $U(\theta)$  function is the open-circuit potential (OCP) corresponding to the local state of charge,  $\theta$ , defined as

$$\theta = \frac{c_s}{c_{s,max}} \quad [15]$$

The experimental OCP dependence on  $\theta$  can be fit to a polynomial function and is used analytically for battery modeling.<sup>51</sup> All lithium concentration ( $c_s, c_e$ ) and potential ( $\phi_s, \phi_e$ ) variables that appear in the Butler-Volmer equation are located at the electrode/electrolyte interface.

Neither potential nor species concentration are continuous across an interface ( $c_s \neq c_e, \phi_s \neq \phi_e$ ). Thus, a total of four interface equations governing interface mass transport and interface current are required. The two equations corresponding to the species transport are

$$\mathbf{n} \cdot (-D_e \nabla c_e) = (1 - t_+) \frac{j}{F} \quad [16]$$

$$\mathbf{n} \cdot (-D_s \nabla c_s) = \frac{j}{F} \quad [17]$$

where  $\mathbf{n}$  is the interface normal vector pointing from the electrode into the electrolyte. Similarly, the two additional interface equations for the potential equations are

$$\mathbf{n} \cdot (\kappa_e \nabla \phi_e + \kappa_D \nabla \ln c_e) = j \quad [18]$$

$$\mathbf{n} \cdot (-\sigma_s \nabla \phi_s) = j \quad [19]$$

**Volume-Averaged transport equations.**—Traditional battery simulation approaches use a volume-averaged model to represent the electrochemistry and transport physics during a battery discharge. Such reduced-order models are necessary as a mesoscale simulation explicitly resolving constituent porous electrode phases on an entire battery cell is computationally infeasible. These traditional volume-averaged models assume that the anode and cathode regions are physically separated (typically by a porous separator); however, this assumption does not hold for interpenetrating microbattery architectures. Therefore, as a natural extension of the recent experimental and mesoscale modeling interest in interpenetrating electrode architectures, the previously presented equations governing the electrochemistry and transport within battery electrodes are volume-averaged assuming that both anode and cathode are present throughout the battery volume, resulting in a three-material volume-averaged battery model.

The procedure used to develop the volume-averaged equations presented here follows that used to develop the original porous electrode theory of Newman and Tiedemann<sup>52</sup> and detailed in Ref. 53. This

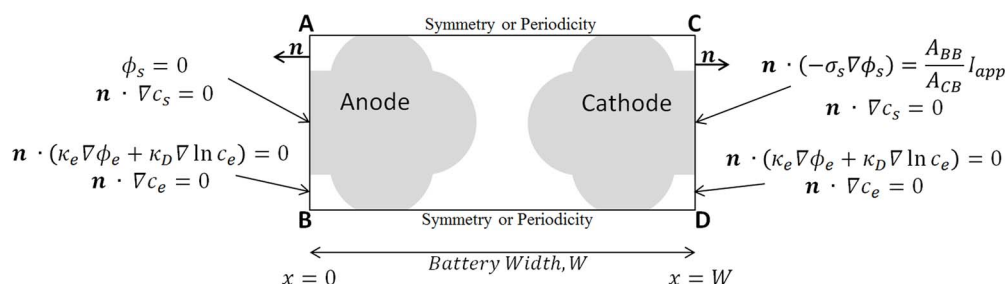


Figure 3. Boundary conditions for battery discharge simulation.

modeling effort is macroscopic in nature and idealizes the geometrical microstructure of the complicated porous electrode transport network. All solution variables are assumed to be continuous and exist at every point in the battery domain. Here we assume that the battery consists of three superimposed continuous regions: anode, cathode, and electrolyte. An REV is used to average the equations and solution variables.<sup>45,51</sup> An REV is a piece of the total structure that is large compared to the feature sizes, but small compared to the overall battery size. For interpenetrating batteries, it is clear that an REV of suitable size must contain anode, cathode, and electrolyte material, as depicted in Figure 2.

The conservation statements presented previously are still valid and volume-averaging over an REV results in the set of scalar transport equations for charge conservation

$$\nabla \cdot (-\sigma_{s,a}^{eff} \nabla \langle \phi_{s,a} \rangle) + a_a \bar{j}_a = 0 \quad [20]$$

$$\nabla \cdot (-\sigma_{s,c}^{eff} \nabla \langle \phi_{s,c} \rangle) + a_c \bar{j}_c = 0 \quad [21]$$

$$\nabla \cdot (-\kappa_e^{eff} \nabla \langle \phi_e \rangle) + \nabla \cdot (-\kappa_D^{eff} \nabla \ln \langle c_e \rangle) - a_a \bar{j}_a - a_c \bar{j}_c = 0 \quad [22]$$

as well as species conservation

$$\frac{\partial (\epsilon_{s,a} \langle c_{s,a} \rangle)}{\partial t} + \nabla \cdot (-D_{s,a}^{eff} \nabla \langle c_{s,a} \rangle) + \frac{a_a \bar{j}_a}{F} = 0 \quad [23]$$

$$\frac{\partial (\epsilon_{s,c} \langle c_{s,c} \rangle)}{\partial t} + \nabla \cdot (-D_{s,c}^{eff} \nabla \langle c_{s,c} \rangle) + \frac{a_c \bar{j}_c}{F} = 0 \quad [24]$$

$$\frac{\partial (\epsilon_e \langle c_e \rangle)}{\partial t} + \nabla \cdot (-D_e^{eff} \nabla \langle c_e \rangle) - (1 - t_+) \frac{a_a \bar{j}_a}{F} - (1 - t_+) \frac{a_c \bar{j}_c}{F} = 0 \quad [25]$$

Subscripts  $s$ ,  $a$ ;  $s$ ,  $c$ ; and  $e$  correspond to values in the solid anode, solid cathode, and electrolyte phases, respectively. Throughout this section brackets are used to indicate a volume-averaged value. Nomenclature is kept consistent with the mesoscale equations:  $\langle c \rangle$  represents volume-averaged lithium concentration, and  $\langle \phi \rangle$  represents volume-averaged electric potential. The transference number  $t_+$  is again assumed to be constant, resulting in the presentation of both 22 and 25 in their simplified form.<sup>45</sup> From the volume-averaging process, material volume fraction ( $\epsilon$ ) is introduced into the unsteady terms of the species equations. We note that the volume averaging process results in six governing equations corresponding to six unknowns at each point in the computational domain ( $\langle \phi_{s,a} \rangle$ ,  $\langle \phi_{s,c} \rangle$ ,  $\langle \phi_e \rangle$ ,  $\langle c_{s,a} \rangle$ ,  $\langle c_{s,c} \rangle$ ,  $\langle c_e \rangle$ ), while typical volume-averaged battery models consist of four ( $\langle \phi_s \rangle$ ,  $\langle \phi_e \rangle$ ,  $\langle c_s \rangle$ ,  $\langle c_e \rangle$ ) due to only one electrode being present in any REV.<sup>38</sup>

Each scalar transport Equations 20–25 contains a diffusion coefficient that is assumed to remain constant. It is important to note that diffusion coefficients in these volume-averaged equations are effective properties and are not intrinsic material properties. Porous electrode theory effective properties are usually estimated using an analytical relationship, with the most common relationship being Bruggeman's approximation.<sup>38,54</sup> This applies to mass diffusivity ( $D$ ), electric conductivity ( $\sigma$ ), and ionic conductivity ( $\kappa$ ), which can be related to corresponding intrinsic properties by

$$D^{eff} = D(\epsilon)^{1.5} \quad [26]$$

$$\sigma^{eff} = \sigma(\epsilon)^{1.5} \quad [27]$$

$$\kappa^{eff} = \kappa(\epsilon)^{1.5} \quad [28]$$

where  $\epsilon$  represents material volume fraction. The diffusional conductivity,  $\kappa_D$ , is included by considering concentrated solution theory and is defined earlier in 4.

One of the major differences between the mesoscale model and the volume-averaged model is the treatment of the Butler-Volmer reaction rate term, defined by 12–15. While the electrochemical reactions take place at electrode/electrolyte phase boundaries as an interface term in a mesoscale model, the volume averaging process removes that

interface geometry and therefore necessarily converts the interface source/sink terms into volumetric terms. The divergence theorem is used to volume-average the Butler-Volmer current density,  $j_k$

$$\iint \nabla \cdot j_k dA_k = a_k \bar{j}_k \quad [29]$$

where  $a_k$  is the specific surface area defined as the ratio of reactive surface area for electrode  $k$  in the REV to the total REV volume and a barred variable ( $\bar{\phantom{x}}$ ) denotes interface values averaged over the entire electrode/electrolyte interface within the REV. For a particle bed, the specific surface area is typically analytically related to particle radius and volume fraction by assuming that the porous electrode is composed of small spheres of a uniform size ( $a = 3\epsilon/r$ ), which is likely not a realistic approximation.<sup>55</sup> Alternatively, surface areas and volumes can be obtained directly from a computational reconstruction of the 3D battery microarchitecture, which is the approach used throughout this paper.

The current density Equations 12–15 require species concentration and potential variables to be electrode/electrolyte interface values. We assume here that for each REV

$$\bar{j}_k = j(\bar{\phi}_{s,k}, \bar{\phi}_e, \bar{c}_{s,k}, \bar{c}_e) \quad [30]$$

where  $k$  again represents a generic electrode type of either anode ( $a$ ) or cathode ( $c$ ) in the transport equations. The relationship between averaged interface surface values required by this equation and volume-averaged values is discussed in the next section.

Boundary and initial conditions for these transport equations directly correspond to those applied to the mesoscale model and depicted in Figure 3 (7–11) by replacing concentration/potential values with their volume-averaged counterparts. For completeness, we present the current collector boundary conditions as

$$\mathbf{n} \cdot \nabla \langle c_{s,a} \rangle = 0 \text{ at } x = 0, W \quad [31]$$

$$\mathbf{n} \cdot \nabla \langle c_{s,c} \rangle = 0 \text{ at } x = 0, W \quad [32]$$

$$\mathbf{n} \cdot \nabla \langle c_e \rangle = 0 \text{ at } x = 0, W \quad [33]$$

$$\mathbf{n} \cdot (-\sigma_{s,c}^{eff} \nabla \langle \phi_{s,c} \rangle) = I_{app} \text{ at } x = W \quad [34]$$

$$\mathbf{n} \cdot \nabla \langle \phi_{s,c} \rangle = 0 \text{ at } x = 0 \quad [35]$$

$$\mathbf{n} \cdot \nabla \langle \phi_{s,a} \rangle = 0 \text{ at } x = W \quad [36]$$

$$\langle \phi_{s,a} \rangle = 0 \text{ at } x = 0 \quad [37]$$

$$\mathbf{n} \cdot (\kappa_e^{eff} \nabla \langle \phi_e \rangle + \kappa_D^{eff} \nabla \ln \langle c_e \rangle) = 0 \text{ at } x = 0, W \quad [38]$$

The other four boundaries in a 3D simulation are considered to be symmetry boundaries (zero flux) for all six field variables.

**Diffusion length method.**—A central focus of the modeling is the relationship between the volume-averaged ( $\langle \phantom{x} \rangle$ ) and surface-averaged ( $\bar{\phantom{x}}$ ) terms. We assume that concentration in the electrolyte and electric potential values are relatively uniform within an REV. Thus, we can define the following variables required by 30 as

$$\bar{\phi}_{s,k} = \langle \phi_{s,k} \rangle \quad [39]$$

$$\bar{\phi}_e = \langle \phi_e \rangle \quad [40]$$

$$\bar{c}_e = \langle c_e \rangle \quad [41]$$

The approach to modeling  $\bar{c}_{s,k}$  is more complex. Solid phase diffusion in the electrode active material can be rate limiting and must be represented accurately in the volume-averaged model.<sup>38</sup> This was a point of emphasis within previous volume-averaged battery modeling work.<sup>48,56</sup> Since we need to simulate batteries with unique electrode microstructural shapes, a method that addresses these electrode shapes is desired. The diffusion length method developed by Wang et al.<sup>48,56</sup> allows for generic treatment of solid phase diffusion by assuming a linear relationship between the solid surface concentration and the volume-averaged concentration within the solid. Using their method

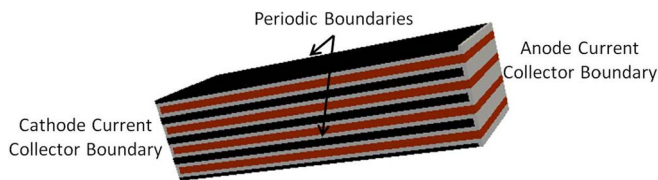


Figure 4: Extruded plates

Figure 4. Extruded plates.

and bearing in mind that our governing equations have been formulated with the convention that  $\bar{j}_k$  is the average interface current density leaving the electrode (see Eqs. 16–19) in direction  $\mathbf{n}$ , introducing the diffusion length ( $l_d$ ) yields the interface relationship

$$\frac{\bar{j}_k}{F} = -D_{s,k} \frac{\partial c_s}{\partial \mathbf{n}} = -D_{s,k} \frac{\bar{c}_{s,k} - \langle c_{s,k} \rangle}{l_{d,k}} \quad [42]$$

for each electrode  $k$ ,<sup>48</sup> where  $l_{d,k}$  is the diffusion length associated with phase  $k$ . As diffusion through the solid material is being modeled, the mass diffusivity ( $D_{s,k}$ ) used here is the intrinsic property value. Solving for  $\bar{c}_{s,k}$  yields a more useful form:

$$\bar{c}_{s,k} = \langle c_{s,k} \rangle - \frac{\bar{j}_k l_{d,k}}{FD_{s,k}} \quad [43]$$

Wang et al. analytically derived the diffusion length for simple shapes by assuming a parabolic concentration profile. They report  $l_d$  values of  $R/5$  for spherical shapes,  $R/4$  for cylindrical shapes, and  $L/3$  for plate-like shapes, where  $R$  is sphere/cylinder radius and  $L$  is plate half-thickness.<sup>48</sup>

It was demonstrated that assuming the previous linear relationship and therefore assuming a steady-state profile introduces significant inaccuracy during the early portion of a discharge when the concentration profile has not yet developed. By comparing their diffusion length method solution to the exact solution obtained from Duhamel's superposition for several simple geometries (sphere, cylinder, plate), Wang et al.<sup>56</sup> improved the model by developing a time-dependent ( $t$ ) correction of the form

$$\bar{c}_{s,k} = \langle c_{s,k} \rangle - \frac{\bar{j}_k l_{d,k}}{FD_{s,k}} \left( 1 - e^{-\frac{4\sqrt{D_{s,k}t}}{3l_{d,k}}} \right) \quad [44]$$

This correction factor was shown to yield consistent error-reducing results for several electrode geometries. Equations 39, 40, 41, and 44 bring closure to 30 and complete the model.

For more complex geometries, there is no simple analytical method to deduce  $l_{d,k}$ . Our approach in these cases is to parametrically sweep through diffusion length values and evaluate error with respect to mesoscale modeling results to determine a suitable diffusion length for each geometry as a function of discharge current.

### 3D Battery Geometries

As previously discussed, interpenetrating electrode configurations have been proposed as a method to improve battery performance by shortening transport path lengths. Here we introduce several interpenetrating electrode configurations that have been proposed and studied previously.<sup>33</sup> Several 2D extrusions that yield 3D interpenetrating batteries are included as simple geometries that lend themselves to additive manufacturing. The first is an alternating plate geometry, shown in Figure 4, where anode and cathode plates alternate with electrolyte filling the gaps between. This figure and subsequent depictions of computational geometries follow the convention that red denotes anode material, black denotes cathode material, and gray denotes electrolyte material. The second extruded geometry considered is an array of cylinders, shown in Figure 5. This 2D geometry is extruded into and out of the page to yield a 3D battery. The anode and cathode current collectors are placed parallel with the page plane on opposite ends of the extruded geometry. This configuration of cylinders was chosen

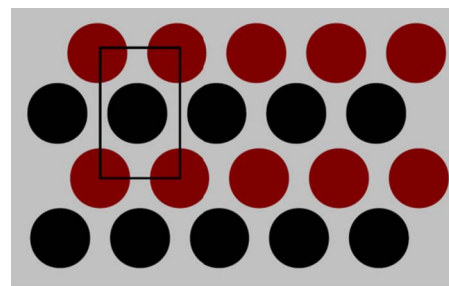


Figure 5. Extruded cylinder array with unit cell outlined.

due to its repeatability and because it exhibits equal volume fractions of anode and cathode active material.

Two 3D electrode geometries that are not 2D extrusions are also introduced. These electrode structures are based on a group of mathematical surfaces defined as minimal surfaces. The two topologies used for this study are the Schwarz P and the gyroid.<sup>57,58</sup> They are triply periodic and define a bi-continuous pore space, thus allowing for an interpenetrating anode/cathode geometry adaptation. For these surface structures, a unit cell is defined as one repeating geometric unit, shown for each geometry in Figure 6.

The Schwarz P surface topology is approximated by  $F_{Schwarz P}(x, y, z) = 0$ , where the Schwarz P function is defined as

$$F_{Schwarz P}(x, y, z) = \cos\left(\frac{2\pi}{L}x\right) + \cos\left(\frac{2\pi}{L}y\right) + \cos\left(\frac{2\pi}{L}z\right) \quad [45]$$

where  $x$ ,  $y$ , and  $z$  are Cartesian coordinates in the physical domain and  $L$  is the cubic unit cell edge length. The gyroid surface topology is approximated by  $F_{gyroid}(x, y, z) = 0$  where the gyroid function is

$$F_{gyroid}(x, y, z) = \sin\left(\frac{2\pi}{L}y\right) \cos\left(\frac{2\pi}{L}z\right) + \sin\left(\frac{2\pi}{L}z\right) \cos\left(\frac{2\pi}{L}x\right) + \sin\left(\frac{2\pi}{L}x\right) \cos\left(\frac{2\pi}{L}y\right) \quad [46]$$

The method used to convert these geometries to interpenetrating battery electrodes has been detailed previously.<sup>33</sup> Setting 45 and 46 equal to a value other than zero represents a surface resembling a hollow shell.<sup>59,60</sup> Considering any evaluation of  $F_{gyroid}(x, y, z)$  greater than a dimensionless thickness parameter ( $t$ ) effectively fills in the shell and results in a solid structure. Using these functions to create anode/electrolyte/cathode interpenetrating structures requires a double Schwarz P and a double gyroid. A double gyroid geometry is obtained when one material is defined by  $F_{gyroid}(x, y, z) > t$  and a second material is defined by  $F_{gyroid}(x, y, z) < -t$ .<sup>60</sup> This same process can be applied to the Schwarz P function to obtain two distinct interpenetrating triply periodic structures. Example electrode representations of these geometries are shown in Figures 7 and 8. Values of  $t$  have been chosen here such that anode and cathode active material volume fractions are approximately equal.

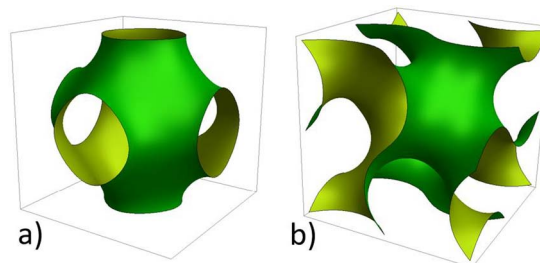


Figure 6. Unit cells of the (a) Schwarz P and (b) gyroid minimal surfaces.

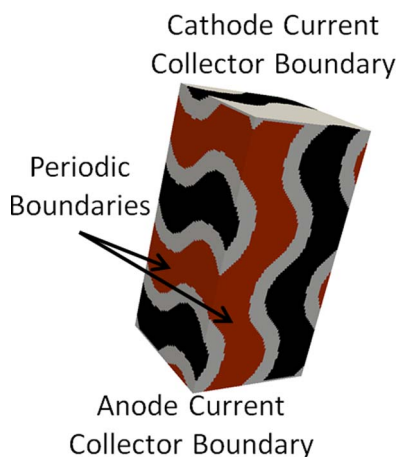


Figure 7. Double gyroid structure with  $t_{anode} = t_{cathode} = 0.6$ .

### Simulation Results and Comparison to Mesoscale Modeling

We simulate discharge performance by incorporating the model and battery geometries presented in the previous sections within the PETSc framework while utilizing a finite volume method (FVM) to discretize the governing equations<sup>61,62</sup> (details included in Appendix). In order to determine the accuracy of the volume-averaged model, we compare discharge simulation results to mesoscale simulation results where constituent-phase geometries are fully resolved.<sup>33</sup> Material and model parameters are presented in Tables I and II, which correspond to a graphite anode and a  $\text{LiMn}_2\text{O}_4$  cathode.<sup>45</sup> Other electrode materials may also be simulated assuming their intrinsic properties and open-circuit potential curves are known. All comparisons are performed on battery geometries with similar widths ( $W = 203 \mu\text{m}$ ) and active material volume fractions ( $\epsilon_{s,a} = \epsilon_{s,c} = 0.325$ ) and therefore exhibit similar theoretical energy densities. The seven discharge rates simulated for each comparison are 5, 10, 20, 40, 80, 160, and 320  $\text{A/m}^2$ , which correspond to C-rates of approximately 0.19C, 0.38C, 0.76C, 1.5C, 3C, 6C, and 12C. While rates of 4C or less are typically considered for traditional applications like powering electric vehicles,<sup>63</sup> 3D battery architectures are commonly pushed to significantly higher rates to assess suitability for applications desiring fast charging capabilities or as supercapacitor alternatives.<sup>22,64</sup>

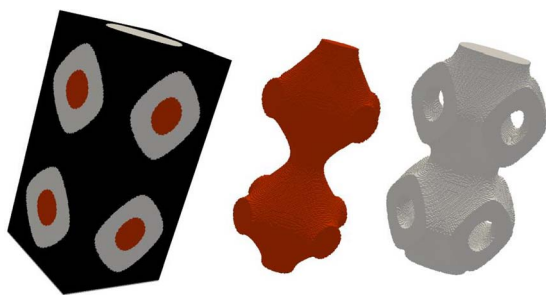


Figure 8. Double Schwarz P structure with  $t_{anode} = t_{cathode} = 0.56$ .

Table II. Model parameters.

Model Parameter	Value
Temperature (K)	300
Li Transport Number, $t_+$	0.363
$\alpha_a, \alpha_c$	0.5
Butler-Volmer Constant, $k$ ( $\text{m}^{2.5}\text{mol}^{-0.5}\text{s}^{-1}$ )	1.10E-11

For simple electrode geometries such as cylinder or plate arrays, analytically derived solid phase diffusion lengths can be used. For more complicated geometries, an appropriate single diffusion length that represents the entire structure is not easily defined, and we investigate several methods for determining a diffusion length for such structures.

**Quantities of interest.**—Two important metrics that we utilize to characterize battery performance are power density and energy density. Energy density represents the total energy supplied by the battery throughout a discharge cycle and power density represents the rate at which that energy is provided. Volumetric power density is obtained from a full battery discharge by

$$\text{Power Density} = \frac{\hat{V} \times I_{app}}{\text{Vol}} \quad [47]$$

where  $\hat{V}$  is time-averaged cell voltage averaged over the entire discharge time,  $I_{app}$  is the constant applied current density, and  $\text{Vol}$  is the total battery volume. Since the anode potential ( $\langle \phi_{s,a} \rangle$ ) is held to a value of 0 volts at the current collector boundary, we define cell voltage ( $V$ ) as the spatially-averaged cathode potential ( $\langle \phi_{s,c} \rangle$ ) at the cathode current collector boundary. Energy density is then evaluated by

$$\text{Energy Density} = \text{Power Density} \times \text{Discharge Time}. \quad [48]$$

In addition to the performance metrics, two geometrical parameters help to describe mesoscale electrode geometries. The first is the previously defined specific surface area ( $a$ ), and the second is *minimum feature size*. When discussed here, feature size refers to the thickness of a particular portion of a structure. The minimum feature size is an important practical geometrical characteristic, since additive manufacturing techniques typically each have a lower limit on feature resolution.

**Extruded geometries: plate and cylinder arrays.**—Since analytical diffusion lengths can be derived for cylinder and plate-like geometries,<sup>48</sup> we first compare the model to mesoscale simulations of these two geometries. We include both a study where surface area to volume ratio is equal across the two geometries as well as a case where the electrode feature sizes (plate thickness and cylinder diameter) are equal.

**Equal surface area.**—We begin with the consideration of an equal surface area to volume ratio ( $a$ ) case, where each electrode geometry exhibits the electrochemical surface area expected from a typical particle-bed geometry. Table III contains information from the mesoscale geometry as well as the microstructural metrics required by the volume-averaged model. The specific electrode surface area value displayed here is calculated directly from the meshed mesoscale geometries by totaling the area of all finite volume faces that reside

Table I. Material properties.<sup>45</sup>

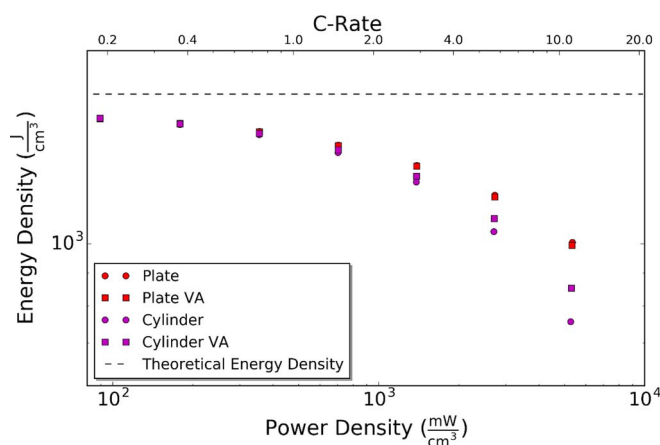
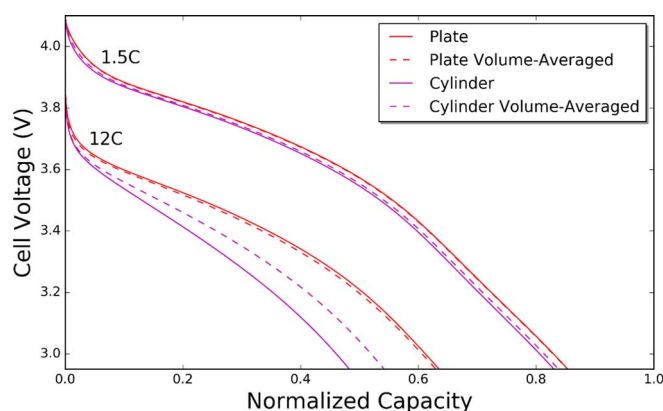
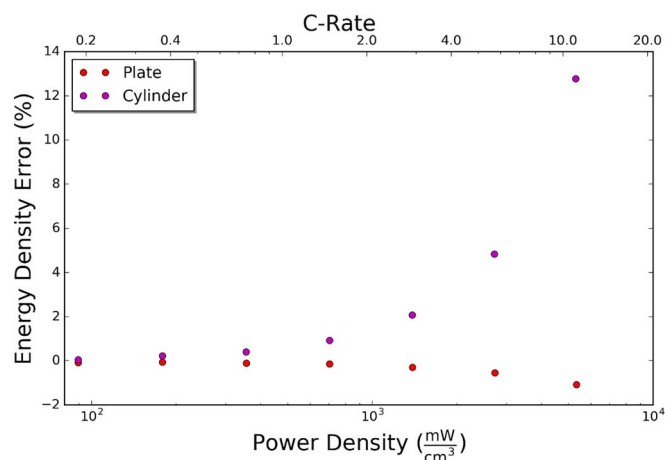
Intrinsic Material Property	$\text{Li}_y\text{Mn}_2\text{O}_4$ Cathode	Electrolyte	$\text{Li}_x\text{C}_6$ Anode
Li/Li <sup>+</sup> Mass Diffusivity, $D$ ( $\text{m}^2/\text{s}$ )	1.00E-13	7.50E-11	3.90E-14
Solid Phase Conductivity, $\sigma_s$ (S/m)	3.8		100
Electrolyte Ionic Conductivity, $\kappa_e$ (S/m)		0.2	
Initial Li Concentration, $c^0$ ( $\text{mol}/\text{m}^3$ )	3900	2000	14780
Maximum Concentration, $c_{s,\text{max}}$ ( $\text{mol}/\text{m}^3$ )	22860		26390

**Table III. Parameters for volume-averaged simulation of simple geometries (equal surface area case).**

Geometry	Electrode Feature Size ( $\mu\text{m}$ )	Diffusion Length ( $l_d$ ) ( $\mu\text{m}$ )	Specific Surface Area ( $a$ ) ( $\mu\text{m}^{-1}$ )
Plate	4.4	0.726	0.149
Cylinder	11	1.375	0.148

between anode and electrolyte and then dividing that total by the REV volume. Since anode and cathode volumes are identical and all geometries are triply periodic, the anode and cathode specific surface areas ( $a_a$ ,  $a_c$ ) both equal the tabulated value. Surface area values may not match theoretical values due to non-conformal meshing. Diffusion length ( $l_d$ ) values are calculated using the analytically derived relations presented previously,<sup>48</sup> where plate half-thickness  $L$  is 2.2  $\mu\text{m}$  and the cylinder radius  $R$  is 5.5  $\mu\text{m}$ .

Figure 9 shows the Ragone plot<sup>65</sup> for the mesoscale model equal surface area comparison. In addition, the volume-averaged results using analytically-derived diffusion lengths are plotted. Discharge curves at two current densities are provided in Figure 10, where we can see the effects of a higher discharge rate on both cell capacity as well as volume-averaged model accuracy. The volume-averaged plate geometry simulation aligns well with the mesoscale simulation throughout the entirety of the discharge in addition to matching the

**Figure 9.** Ragone plot for the equal surface area case including volume-averaged (VA) results in addition to mesoscale results.**Figure 10.** Comparison of mesoscale and volume-averaged discharge curves for both plate and cylinder battery geometries with equal electrode surface area. Since these discharges are theoretically anode limited due to electrode volume fractions and initial conditions, normalized capacity here is equivalent to anode utilization.**Figure 11.** Errors in volume-averaged model energy density with respect to a mesoscale model for an equal surface area case.

time-integrated energy density value observed in Figure 9. The models do not agree as well when simulating the cylinder geometry, where the volume-averaged discharge curves over-predict energy density when compared to the mesoscale model predictions, particularly at high discharge rates.

The relative errors in energy density between the two models are presented in Figure 11. Errors for the plate geometry are quite low, staying within  $\pm 2\%$  of the mesoscale results. The cylinder geometry shows more significant deviation from the mesoscale model at higher discharge rates, although errors stay within  $\sim 2\%$  even up to a 3C discharge rate, which is a reasonable sacrifice to make when using a reduced-order model and thus gaining the ability to simulate full batteries. One likely source for the error in both geometries is the assumption of a parabolic concentration profile during the derivation of a diffusion length.<sup>48</sup> The corrective term introduced in 44 could also be less effective at high rates. A second source of error for the cylinder geometry may be in the mesoscale mesh resolution, although mesh refinement studies show energy density errors due to spatial discretization of only  $\sim 1\%$ . Lastly, the diffusion length of the cylinder geometry is almost double that of the plate geometry. A longer diffusion length likely also contributes to the breakdown in the parabolic profile assumption.

**Equal electrode feature size.**—We next perform a comparison to an equal electrode feature size case, where each battery geometry is scaled such that its electrode feature size (plate thickness, cylinder diameter) is 10  $\mu\text{m}$ . This comparison may be more relevant due to feature resolution limits for additive manufacturing techniques. We focus on the electrode size here since manufacturing these simple extruded geometries would likely involve building up both the anode and cathode materials.<sup>24–29</sup> Table IV contains the microstructural summary required by the volume-averaged model with diffusion lengths once again calculated using the derived relations.

Figures 12 and 13 show several discharge curves as well as errors in energy density for the uniform electrode feature size case. In the previous case (uniform surface area, Figure 11), the cylinder diameter was similar (11  $\mu\text{m}$  vs. 10  $\mu\text{m}$ ), so the observed similar

**Table IV. Parameters for volume-averaged simulation of simple geometries (equal electrode feature size case).**

Geometry	Electrode Feature Size ( $\mu\text{m}$ )	Diffusion Length ( $l_d$ ) ( $\mu\text{m}$ )	Specific Surface Area ( $a$ ) ( $\mu\text{m}^{-1}$ )
Plate	10	1.6667	0.066
Cylinder	10	1.25	0.169

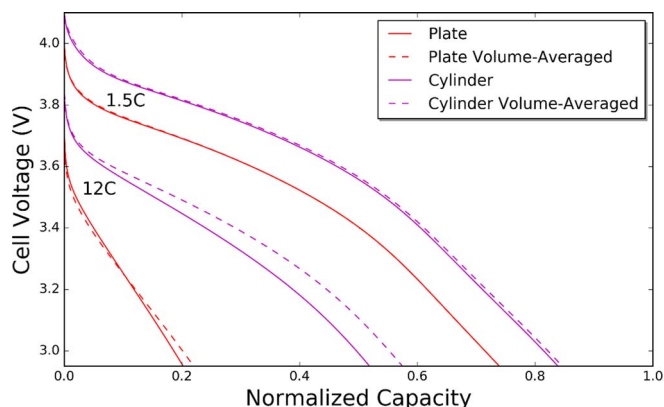


**Figure 12.** Discharge curves for both the plate and cylinder geometries at several discharge rates for the equal electrode feature size case. Since these discharges are theoretically anode limited due to electrode volume fractions and initial conditions, normalized capacity here is equivalent to anode utilization.

behavior for that geometry in Figure 13 is expected. Interestingly, when plate thickness and cylinder diameter are comparable, volume-averaged errors of the same order are observed, indicating that the main source of error at the higher discharge rates is likely the feature size (diffusion length) and not an error in model form between plates and cylinders. We observe very tolerable errors of less than 2% up to 3C discharge rates, although error increases steeply as rates are pushed beyond 3C. Even so, errors are only about 8–12% even at very high discharge rates (12C), indicating that our volume-averaged model can produce adequate estimates for engineering design.

The cylinder geometry does show a relatively consistent, slightly higher error when compared to the plate geometry. This behavior is likely the result of lithium-ion gradients in the electrolyte, which are certainly more pronounced at higher discharge rates. While the model does account for lithium-ion gradients across the battery cell, we neglect any gradient between the anode and cathode within an REV with 41. When comparing these two geometries, our previous mesoscale simulation work demonstrated that ion gradients between electrodes within an REV are much more significant and non-uniform in the cylinder geometry due to the variable distance from anode to cathode inherent in the geometric design.<sup>33</sup> Additionally, we have employed typical relations for effective ionic and electronic conductivity/diffusivity (Eqs. 26–28). It is quite likely that these relations are not accurate for certain geometries.<sup>55</sup> If these effective property relations are overestimating effective transport (underestimating pore phase tortuosity), they could very well be the cause of the volume-

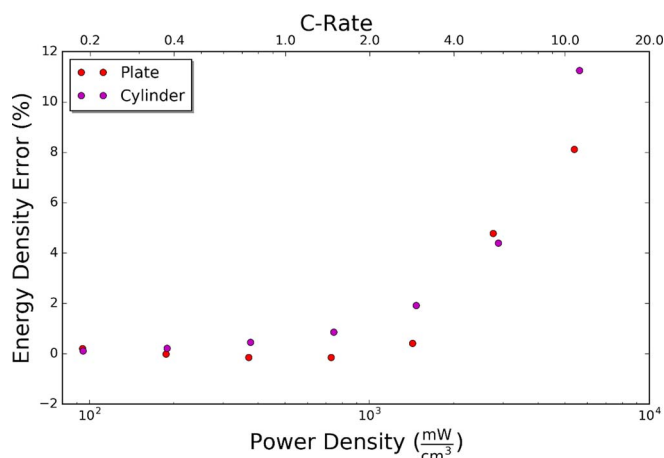


**Figure 13.** Errors in volume-averaged model energy density with respect to mesoscale model for an equal electrode feature size case.

**Table V. Parameters for volume-averaged simulation of minimal surface geometries (equal surface area case).**

Geometry	Electrode Feature Size ( $\mu\text{m}$ )	Specific Surface Area ( $a$ ) ( $\mu\text{m}^{-1}$ )
Gyroid	10.5	0.147
Schwarz P	7.5	0.150

averaged model over-predicting performance at high C-rates where ionic transport limitations within the electrolyte become relevant. This observation does not indicate that cylinder arrays are inferior to plate designs, but does cause the assumption of uniform lithium-ion surface concentration around the electrode cylinders and/or the assumption of typical Bruggeman effective transport to become less valid.

**Minimal surface geometries: gyroid and schwarz P.**—While diffusion lengths can be easily calculated for symmetric shapes like cylinders, spheres, or plates, 3D batteries with no axis of symmetry present a more complicated scenario. Furthermore, these shapes vary in thickness throughout the battery, making the calculation of one single diffusion length difficult. In order to determine a diffusion length that most closely reflects mesoscale simulations, we investigate the error profile of a range of diffusion lengths for both the gyroid and Schwarz P geometries. We consider two cases here: a uniform surface area case as well as a minimum electrolyte feature size (anode to cathode separation distance) case.

**Equal surface area.**—As in the previous section, we first consider the equal surface area case. Relevant volume-averaged microstructure parameters are summarized in Table V and error plots similar to Figures 11 and 13 are presented for both geometries for a range of

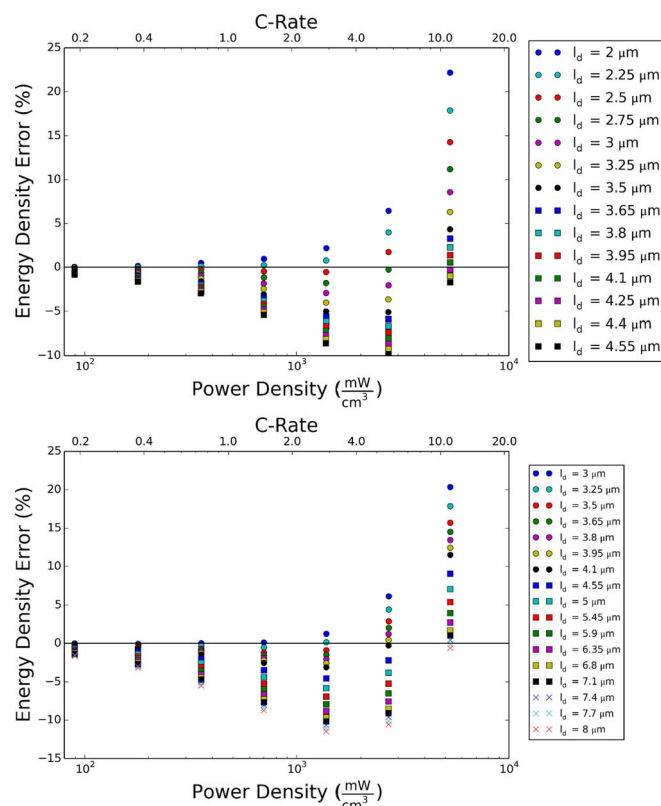


**Figure 14.** Error in volume-averaged energy density for both the gyroid (top) and Schwarz P (bottom) geometries for a range of diffusion lengths.

diffusion lengths in Figure 14. To maintain readability, not all diffusion lengths simulated are plotted in this figure.

Both geometries show a range of errors at each discharge rate. As expected, large diffusion lengths correspond to a lower energy density, resulting in negative relative errors. At high power densities, we see a positive relative error for most diffusion lengths, indicating that the volume-averaged model is overpredicting performance at those lengths. From this group of simulations, we can determine the diffusion length that best matches the mesoscale simulation by considering the L2-norm error for each length. The L2-norm error is represented by

$$L2 = \sqrt{\sum_{k=1}^n |E_k|^2} \quad [49]$$

where  $n$  represents the number of data points for each diffusion length ( $n = 7$  here), and  $E_k$  is the relative error percentage at point  $k$ .

Furthermore, we can report the diffusion length that minimizes L2-norm for several ranges of simulated discharge currents, as shown in Table VI. For the entire range of discharge current densities considered, a gyroid  $l_d$  value of 3.25  $\mu\text{m}$  and a Schwarz P  $l_d$  value of 4.7  $\mu\text{m}$  correspond to the lowest observed L2-norm. In general, L2-norms remain small for all current density ranges less than 80  $\text{A}/\text{m}^2$  (3C), and at these low-error discharge rates a gyroid  $l_d$  value of 2.25  $\mu\text{m}$  and a Schwarz P value of 3.0  $\mu\text{m}$  are quite accurate ( $<3\%$  error). If we consider the electrode feature sizes, defined as the minimum electrode thickness in the domain and presented in Table V, these  $l_d$  values correspond to roughly  $R/2.33$  and  $R/1.25$  for the gyroid and Schwarz P, respectively.  $R$  is defined as the minimum feature size half-length for consistency with the simple geometries discussed in the previous section. While an  $l_d$  relation more closely resembling the cylindrical or plate values of  $R/4$  and  $L/3$  might be expected, the  $l_d$  relations here are likely higher due to the  $R$  value being based on the minimum electrode thickness. Calculating and using a spatially averaged (larger)  $R$  value would result in higher denominator values in the gyroid and Schwarz P  $l_d$  relations.

In addition to the Ragone-like error plot, we plot the error results for each simulated discharge current as a function of diffusion length in Figure 15. We observe more clearly here that an increase in diffusion length results in a lower energy density, and that for each discharge current, there is a corresponding zero-error diffusion length. Linearly interpolated zero-error diffusion lengths for each discharge current density are supplied in Table VII and visualized in Figure 16. An exponential least squares curve fit and corresponding equation is included in the figure to allow for more convenient use of these results. This figure helps to demonstrate that at these feature sizes, a single diffusion length can be accurately used for discharge rates less than approximately 80  $\text{A}/\text{m}^2$  (3C). To summarize, if one wishes to use a single diffusion length for a range of discharge currents, the appropriate value from Table VI should be used. For more accuracy within the range of discharge rates simulated here, the exponential curve fits displayed in Figure 16 should be used.

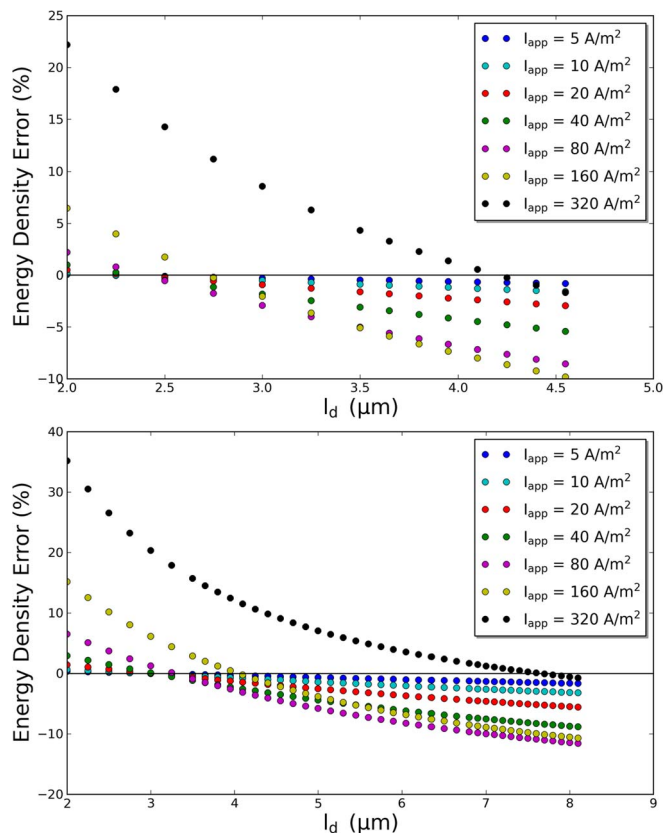


**Figure 15.** Volume-averaged errors in energy density vs diffusion length for both the gyroid (top) and Schwarz P (bottom) geometries (equal surface area case).

*Equal electrolyte feature size.*—To push the limits of the model, we consider a case where the minimum separation distance between anode and cathode (electrolyte feature size) must be 10  $\mu\text{m}$ . Relevant geometrical information is presented in Table VIII, where we see that such a requirement results in larger electrode feature sizes than the previous studies, which were all 11  $\mu\text{m}$  or smaller. A Ragone-like error plot similar to Figure 14 is not included here for brevity, but error-minimizing diffusion lengths for various discharge rates are likewise provided in Table IX. Unlike in the equal surface area case, we do not see any range where a constant diffusion length yields the lowest error. Due to the increased feature sizes when compared to the equal surface area case ( $\sim 2.5\times$  increase), it is likely that these geometries are no longer within a range for which the diffusion length model is accurate. To get the most accurate single diffusion length within a given discharge range, Table IX can still be used.

Error plots similar in form to Figure 15 can be found in Figure 17, where significantly different behavior is observed. We see that for the

**Table VI.** Diffusion lengths that result in the lowest observed L2-norm (equal surface area case).

$I_{app}$ (A/m <sup>2</sup> ) Range	Gyroid		Schwarz P	
	Min. Error $l_d$ ( $\mu\text{m}$ )	L2-norm (%)	Min. Error $l_d$ ( $\mu\text{m}$ )	L2-norm (%)
5–5	2.25	0.03	3	0.00
5–10	2.25	0.03	3	0.06
5–20	2.25	0.13	3	0.06
5–40	2.25	0.28	3	0.12
5–80	2.5	0.77	3.25	0.70
5–160	2.5	1.90	3.65	3.11
5–320	3.25	8.80	4.7	11.13

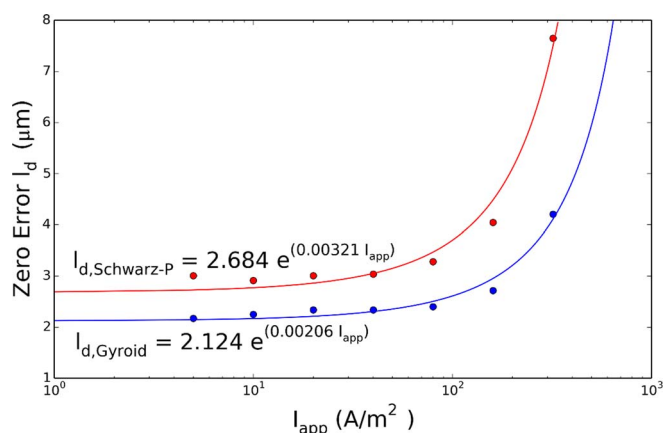
**Table VII. Linearly interpolated zero-error diffusion lengths for each discharge current (equal surface area case).**

$I_{app}$ (A/m <sup>2</sup> )	Gyroid $l_d$ (μm)	Schwarz P $l_d$ (μm)
5	2.17	3.01
10	2.25	2.91
20	2.34	3.01
40	2.34	3.04
80	2.40	3.28
160	2.72	4.04
320	4.20	7.65

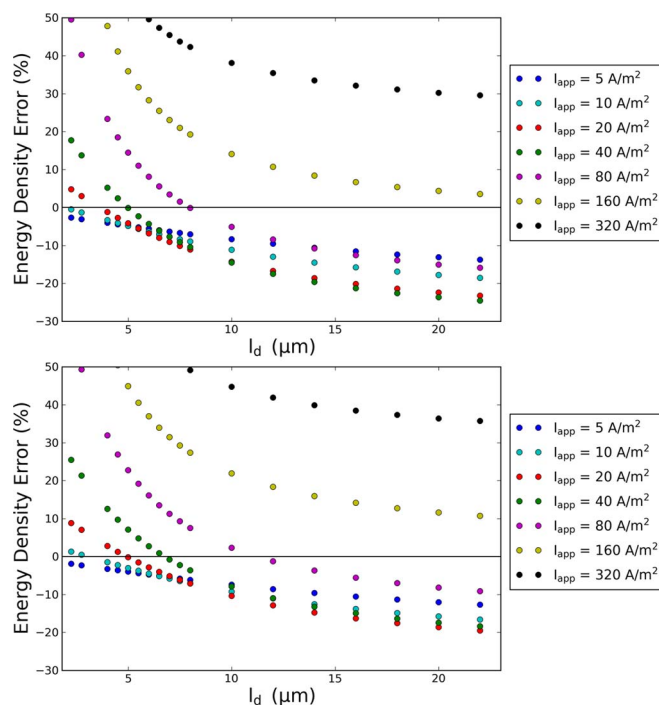
lowest discharge current of 5 A/m<sup>2</sup>, there is no point where the volume-averaged model overpredicts energy density (i.e. where it crosses the zero error line), even when considering a diffusion length value of 0 μm. Conversely, there is no point where the volume-averaged energy density underpredicts the energy density (i.e. crosses the zero-error line) for the two largest discharge currents, as they approach an asymptote at an error greater than zero. It appears that the volume-averaged diffusion length model developed is not well-suited for such large electrode feature sizes and/or low surface area structures likely in part to the breakdown in the parabolic profile assumption. These plots clearly show that the estimated diffusion length relations of  $R/2.33$  and  $R/1.25$  for the gyroid and Schwarz P, respectively, may not hold for larger feature sizes. Additional studies at various feature sizes could be helpful in determining the effect of specific surface area ( $a$ ) and therefore feature size on the diffusion length correlation for gyroid and Schwarz P microstructures. For completeness, linearly interpolated zero-error diffusion lengths are provided for discharge currents where they exist in Table X, and again plotted along with exponential curve fits in Figure 18.

## Conclusions

A 3D interpenetrating battery volume-averaged electrochemical transport model has been developed and numerically implemented in

**Figure 16.** Zero-error diffusion lengths vs discharge current density for gyroid (blue) and Schwarz P (red) geometries including exponential curve fits (equal surface area case).**Table VIII. Parameters for volume-averaged simulation of minimal surface geometries (equal electrolyte feature size case).**

Geometry	Electrode Feature Size (μm)	Specific Surface Area ( $a$ ) (μm <sup>-2</sup> )
Gyroid	23.86	0.0649
Schwarz P	16.67	0.067

**Figure 17.** Volume-averaged errors in energy density vs diffusion length for both the gyroid (top) and Schwarz P (bottom) geometries (equal electrolyte feature size case).

PETSc using the finite volume method (FVM). The model assumes anode, cathode, and electrolyte all exist in each representative elemental volume (REV), and thus results in a system of six scalar transport equations. The equations are coupled through an interface-averaged Butler-Volmer reaction, and concentration gradients in the electrodes are approximated by the diffusion length method. While not exact, this method is generic in that it does not require any analytically derived concentration profiles, allowing complex geometries to be simulated. By comparing to mesoscale simulations, we show that the model is quite accurate for simple geometries such as interdigitated plates and cylinders when analytically derived diffusion length relationships are used.

For discharge rates up to 3C, relative energy density errors remain within  $\sim 2\%$  for surface areas and electrode feature sizes comparable to typical modern electrode particles (4.4-11 μm). Capturing mesoscale behavior of complicated non-uniform 3D battery microstructures in a volume-averaged model is expected to be more difficult. However, for the smaller feature size (7.5-10.5 μm) minimal surface geometry batteries, we observe that a single diffusion length value of approximately  $R/2.33$  and  $R/1.25$  for the gyroid and Schwarz P geometries, respectively, can be used without introducing significant error ( $< 3\%$ ) for discharge rates up to 3C (80 A/m<sup>2</sup>), with  $R$  representing the minimum feature size half-length. Disappointingly, we observe no such consistent value for the larger feature size (17-24 μm) structures, and conclude that the limitations of the volume-averaged diffusion length model become very evident in these larger geometries, especially for higher discharge rates. In summary, for discharge rates up to 3C, we show that the 3D battery volume-averaged model developed here can quite accurately simulate 3D battery electrodes that are sized to compete with particle-bed electrodes using a single diffusion length for each geometry. Such a model makes 3D battery simulations on the full-battery scale possible without sacrificing significant accuracy.

Several 3D battery microstructures are considered here, but this is only a small sample of possible architectures. There are many cutting edge manufacturing techniques resulting in interesting geometries with potential for battery electrode applications. The additive manufacturing field is advancing quickly, and microbatteries with very small

**Table IX.** Diffusion lengths that result in the lowest observed L2-norm (equal electrolyte feature size case).

$I_{app}$ (A/m <sup>2</sup> ) Range	Gyroid		Schwarz P	
	Min. Error $l_d$ (μm)	L2-norm (%)	Min. Error $l_d$ (μm)	L2-norm (%)
5–5	0	0.92	0	0.17
5–10	1.5	2.24	2.25	2.30
5–20	2.75	4.52	4.5	4.46
5–40	4.5	7.07	6	7.63
5–80	6	14.21	7.5	14.32
5–160	8	27.05	10	28.22
5–320	12	47.79	16	50.00

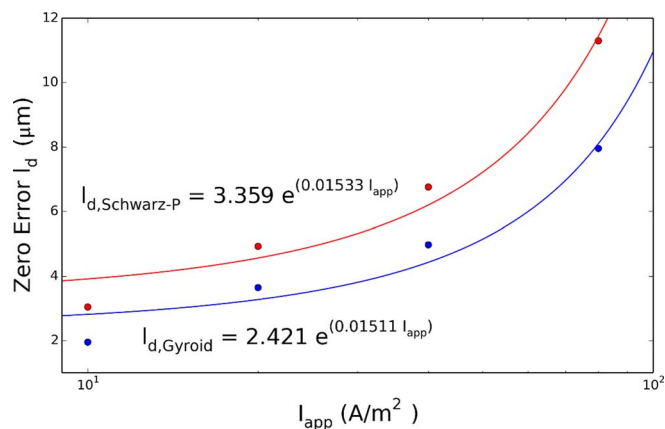
**Table X.** Linearly interpolated zero-error diffusion lengths for each discharge current (equal electrolyte feature size case).

$I_{app}$ (A/m <sup>2</sup> )	Gyroid $l_d$ (μm)	Schwarz P $l_d$ (μm)
5	-	-
10	1.96	3.05
20	3.65	4.93
40	4.98	6.76
80	7.96	11.30
160	-	-
320	-	-

features have already been manufactured and tested.<sup>24,21</sup> Our model and PETSc implementation can easily be utilized to simulate geometries that were not considered as part of this work. Additionally, the anode, cathode, and electrolyte materials simulated are only one of many possible material sets that are commonly used for lithium-ion batteries.<sup>4</sup> Adding a new material to our model would be a straightforward extension, assuming intrinsic transport properties and open circuit potential curve-fits could be obtained for each electrode material. The present work may be extended by including the thermal effects of battery charge/discharge. Significant heat is generated at the electrode/electrolyte interface due to the reactions taking place there, and Joule heating takes place throughout the battery.<sup>66,56</sup> Additionally, experimental validation would both provide confidence in the model as well as demonstrate the feasibility of manufacturing the minimal surface geometries studied here.

### Acknowledgment

We would like to thank Eric Duoss and others at Lawrence Livermore National Laboratory for their insight into microbattery manufac-

**Figure 18.** Zero-error diffusion lengths vs. discharge current density for gyroid (blue) and Schwarz P (red) geometries including exponential curve fits (equal electrolyte feature size case).

turing and design. We also acknowledge the Sandia National Laboratories Campus Executive Fellowship Laboratory Directed Research and Development (LDRD) program at the University of Texas at Austin for financial support of this research. Sandia National Laboratories is a multi-mission laboratory managed and operated by National Technology and Engineering Solutions of Sandia, LLC, a wholly owned subsidiary of Honeywell International, Inc., for the U.S. Department of Energy's National Nuclear Security Administration under contract DE-NA0003525. This paper describes objective technical results and analysis. Any subjective views or opinions that might be expressed in the paper do not necessarily represent the views of the U.S. Department of Energy or the United States Government.

### Appendix

**Numerical Implementation.**—A cell-centered finite volume method (FVM) is applied to scalar transport governing Equations 20–25 to yield a discretized set of equations. We employ a standard FVM formulation,<sup>67,68</sup> so implementation details are not included here. The volume-averaged model contains six scalar transport equations or field variables ( $\langle c_{s,a} \rangle$ ,  $\langle c_{s,c} \rangle$ ,  $\langle c_e \rangle$ ,  $\langle \phi_{s,a} \rangle$ ,  $\langle \phi_{s,c} \rangle$ ,  $\langle \phi_e \rangle$ ), while typical mesoscale models only consist of two at each point in the computational domain ( $c$  and  $\phi$ ), except at material interfaces where concentration and electric potential can be discontinuous.<sup>33</sup> However, since the microstructure does not need to be resolved, the volume-averaged model operates on much coarser meshes, resulting in significantly fewer total degrees of freedom in the physical domain.

The volume-averaged model can be solved in a fully-coupled stable algorithm on a hexahedral mesh, which we have implemented in the PETSc framework.<sup>61,62</sup> There is strong inter-equation coupling here as each equation contains a nonlinear  $\bar{j}_k$  term. A fully analytic Jacobian matrix is computed, and a Newton method with line search is used with a stabilized biconjugate gradient iterative linear solver. The boomerang algebraic multigrid preconditioner from the Hypre add-on package is also used to accelerate the convergence of the linear solver. By nature of volume-averaging, the only microstructural information required by the model are volume fractions ( $\epsilon_e$ ,  $\epsilon_{s,a}$ ,  $\epsilon_{s,c}$ ), electrode surface area to volume ratios ( $a_a$ ,  $a_c$ ), and electrode diffusion lengths ( $l_{d,a}$ ,  $l_{d,c}$ ). The battery is considered discharged when the potential difference across the current collector boundaries reaches a value less than 2.95 volts.

Each battery discharge simulation is discretized into approximately 2000–5000 time steps and solved over hundreds of finite volume cells, resulting in typical simulation run times of a few minutes on one computational core for low discharge currents. This corresponds to a minimum of three orders of magnitude speedup when comparing to the corresponding mesoscale-resolved simulations previously published,<sup>33</sup> which typically ranged from 2 to 18 hours of run time on 36–48 CPU cores. This is largely due to the mesoscale simulations requiring  $\sim 800,000$  finite volume cells to achieve numerical accuracy and adequate geometrical representation, resulting in  $\sim 1000$  times the number of unknowns in the simulation. Due to the highly nonlinear nature of the Butler-Volmer current equation, the prevailing  $\bar{j}_k$  value used in 44 was under-relaxed. Under-relaxation coefficient ( $\alpha$ ) values ranging from 0.15–0.3 provided the most stable convergence depending on discharge current.<sup>67</sup> Even though the source terms in Eqs. 20–25 also contain  $\bar{j}_k$ , underrelaxation there was not necessary. We also found that a gradual ramp-up of the  $l_d$  value during the first time step allowed for stable behavior for all simulations performed. While we did not focus on simulation runtime performance, it would likely improve with optimization of these numerical techniques.

### ORCID

Bradley L. Trembacki <https://orcid.org/0000-0001-8742-3679>  
Scott A. Roberts <https://orcid.org/0000-0002-4196-6771>

## References

- M. Wakihara and O. Yamamoto, *Lithium ion batteries: fundamentals and performance*, John Wiley & Sons (2008).
- M. Armand and J.-M. Tarascon, *Nature*, **471**(7179), 652 (2008).
- J. B. Goodenough, *Annu. Rev. Mater. Res.*, **33**(1), 91 (2003).
- A. Manthiram, *J. Phys. Chem. Lett.*, **2**(3), 176 (2011).
- J. B. Goodenough and Y. Kim, *Chem. Mater.*, **22**(3), 587 (2009).
- V. Etacheri, R. Marom, R. Elazari, G. Salitra, and D. Aurbach, *Energy Environ. Sci.*, **4**(9), 3243 (2011).
- G. Girishkumar, B. McCloskey, A. C. Luntz, S. Swanson, and W. Wilcke, *J. Phys. Chem. Lett.*, **1**(14), 2193 (2010).
- P. P. Mukherjee, S. Pannala, and J. A. Turner, *Modeling and Simulation of Battery Systems*, chapter 25, pp. 841. Wiley-Blackwell (2011).
- J. Newman, K. E. Thomas, H. Hafezi, and D. R. Wheeler, *J. Power Sources*, **119**, 838 (2003).
- U. S. Kim, C. B. Shin, and C.-S. Kim, *J. Power Sources*, **189**(1), 841 (2009).
- A. Manthiram, *Battery Applications*, John Wiley & Sons, Inc. (2002).
- H. Zheng, L. Zhang, G. Liu, X. Song, and V. S. Battaglia, *J. Power Sources*, **217**(0), 530 (2012).
- J. Newman and K. E. Thomas-Alyea, *Electrochemical systems*, John Wiley & Sons (2012).
- T. Drezzen, N.-H. Kwon, P. Bowen, I. Teerlinck, M. Isono, and I. Exnar, *J. Power Sources*, **174**(2), 949 (2007).
- Y.-H. Chen, C.-W. Wang, X. Zhang, and A. M. Sastry, *J. Power Sources*, **195**(9), 2851 (2010).
- G. Liu, H. Zheng, A. S. Simens, A. M. Minor, X. Song, and V. S. Battaglia, *J. Electrochem. Soc.*, **154**(12), A1129 (2007).
- H. Zheng, G. Liu, X. Song, P. Ridgway, S. Xun, and V. S. Battaglia, *J. Electrochem. Soc.*, **157**(10), A1060 (2010).
- D. Guy, B. Lestriez, R. Bouchet, and D. Guyomard, *J. Electrochem. Soc.*, **153**(4), A679 (2006).
- J.-M. Tarascon and M. Armand, *Nature*, **414**(6861), 359 (2001).
- J. W. Long, B. Dunn, D. R. Rolison, and H. S. White, *Chem. Rev.*, **104**(10), 4463 (2004).
- J. H. Pikul, H. G. Zhang, J. Cho, P. V. Braun, and W. P. King, *Nature Commun.*, **4**, 1732 (2013).
- C. Zhu, T. Liu, F. Qian, W. Chen, S. Chandrasekaran, B. Yao, Y. Song, E. B. Duoss, J. D. Kuntz, C. M. Spadaccini, M. A. Worsley, and Y. Li, *Nano Today*, **15**, 107 (2017).
- J. Li, M. C. Leu, R. Panat, and J. Park, *Mater. Des.*, **119**, 417 (2017).
- K. Sun, T.-S. Wei, B. Y. Ahn, J. Y. Seo, S. J. Dillon, and J. A. Lewis, *Adv. Mater.*, **25**(33), 4539 (2013).
- C. L. Cobb and C. C. Ho, *Electrochem. Soc. Interface*, **25**(1), 75 (2016).
- H.-S. Min, B. Y. Park, L. Taherabadi, C. Wang, Y. Yeh, R. Zaouk, M. J. Madou, and B. Dunn, *J. Power Sources*, **178**(2), 795 (2008).
- F. Chamran, Y. Yeh, H.-S. Min, B. Dunn, and C.-J. Kim, *J. Microelectromech. Syst.*, **16**(4), 844 (2007).
- T. S. Arthur, D. J. Bates, N. Cirigliano, D. C. Johnson, P. Malati, J. M. Mosby, E. Perre, M. T. Rawls, A. L. Prieto, and B. Dunn, *MRS Bulletin*, **36**(7), 523 (2011).
- L. Baggetto, R. A. Niessen, F. Roozeboom, and P. H. Notten, *Adv. Funct. Mater.*, **18**(7), 1057 (2008).
- G. B. Less, J. H. Seo, S. Han, A. M. Sastry, J. Zausch, A. Latz, S. Schmidt, C. Wieser, D. Kehrwald, and S. Fell, *J. Electrochem. Soc.*, **159**(6), A697 (2012).
- T. Hutzenlaub, S. Thiele, N. Paust, R. Spotnitz, R. Zengerle, and C. Walchshofer, *Electrochim. Acta*, **115**(0), 131 (2014).
- S. A. Roberts, H. Mendoza, V. E. Brunini, B. L. Trembacki, D. R. Noble, and A. M. Grillet, *J. Electrochem. Energy Convers. Storage*, **13**(3), 031005 (2016).
- B. Trembacki, E. Duoss, G. Oxberry, M. Stadermann, and J. Murthy, *J. Electrochem. Soc.*, **166**(6), A923 (2019).
- B. L. Trembacki, D. R. Noble, V. E. Brunini, M. E. Ferraro, and S. A. Roberts, *J. Electrochem. Soc.*, **164**(11), E3613 (2017).
- A. N. Mistry, K. Smith, and P. P. Mukherjee, *ACS Appl. Mater. Interfaces*, **10**(7), 6317 (2018).
- E. M. Ryan and P. P. Mukherjee, *Prog. Energy Combust. Sci.*, **71**, 118 (2019).
- M. Doyle and J. Newman, *Electrochim. Acta*, **40**(13-14), 2191 (1995).
- M. Doyle, T. F. Fuller, and J. Newman, *J. Electrochem. Soc.*, **140**(6), 1526 (1993).
- W. B. Gu and C. Y. Wang, *J. Electrochem. Soc.*, **147**(8), 2910 (2000).
- P. M. Gomadam, J. W. Weidner, R. A. Dougal, and R. E. White, *J. Power Sources*, **110**(2), 267 (2002).
- S. Allu, S. Kalnaus, S. Simunovic, J. Nanda, J. Turner, and S. Pannala, *J. Power Sources*, **325**, 42 (2016).
- G.-H. Kim, K. Smith, J. Lawrence-Simon, and C. Yang, *J. Electrochem. Soc.*, **164**(6), A1076 (2017).
- P. De Vidts and R. E. White, *J. Electrochem. Soc.*, **144**(4), 1343 (1997).
- A. Vadakkepatt, B. Trembacki, S. R. Mathur, and J. Y. Murthy, *J. Electrochem. Soc.*, **163**(2), A1 (2016).
- M. Doyle, J. Newman, A. S. Gozdz, C. N. Schmutz, and J. Tarascon, *J. Electrochem. Soc.*, **143**(6), 1890 (1996).
- V. R. Subramanian, V. D. Diwakar, and D. Tapriyal, *J. Electrochem. Soc.*, **152**(10), A2002 (2005).
- V. Ramadesigan, V. Boovaragavan, J. C. Pirkle, and V. R. Subramanian, *J. Electrochem. Soc.*, **157**(7), A854 (2010).
- C. Wang, W. Gu, and B. Liaw, *J. Electrochem. Soc.*, **145**(10), 3407 (1998).
- R. W. Hart, H. S. White, B. Dunn, and D. R. Rolison, *Electrochem. Commun.*, **5**(2), 120 (2003).
- V. Zadin, H. Kasemägi, A. Aabloo, and D. Brandell, *J. Power Sources*, **195**(18), 6218 (2010).
- T. F. Fuller, M. Doyle, and J. Newman, *J. Electrochem. Soc.*, **141**(1), 1 (1994).
- J. Newman and W. Tiedemann, *AIChE Journal*, **21**(1), 25 (1975).
- I. Nozad, R. Carbonell, and S. Whitaker, *Chem. Eng. Sci.*, **40**(5), 843 (1985).
- V. D. Bruggeman, *Annalen der Physik*, **416**(7), 636 (1935).
- B. L. Trembacki, A. N. Mistry, D. R. Noble, M. E. Ferraro, P. P. Mukherjee, and S. A. Roberts, *J. Electrochem. Soc.*, **165**(13), E725 (2018).
- C. Wang and V. Srinivasan, *J. Power Sources*, **110**(2), 364 (2002).
- A. H. Schoen, Infinite periodic minimal surfaces without self-intersections. Technical Report NASA Technical Note TN D-5541, NASA (1970).
- S. Torquato, S. Hyun, and A. Donev, *Phys. Rev. Lett.*, **89**(26), 266601 (2002).
- M. Wohlgenuth, N. Yufa, J. Hoffman, and E. L. Thomas, *Macromolecules*, **34**(17), 6083 (2001).
- M. R. J. Scherer, *Double-Gyroid-Structured functional materials: synthesis and applications*, Springer Science & Business Media (2013).
- S. Balay, J. Brown, K. Buschelman, V. Eijkhout, W. Gropp, D. Kaushik, M. Knepley, L. C. McInnes, B. F. Smith, and H. Zhang, *Petsc users manual. technical report an195/11 - revision 3.3*. Technical report, Argonne National Laboratory (2013).
- S. Balay, W. D. Gropp, L. C. McInnes, and B. F. Smith, In *Modern software tools for scientific computing*, pp. 163. Springer (1997).
- K. Smith and C.-Y. Wang, *J. Power Sources*, **160**(1), 662 (2006).
- J. Ye, A. C. Baumgaertel, Y. M. Wang, J. Biener, and M. M. Biener, *ACS nano*, **9**(2), 2194 (2014).
- D. V. Ragone, Review of battery systems for electrically powered vehicles. Technical report, *SAE Technical Paper* (1968).
- J. Newman, *Ind. Eng. Chem. Res.*, **34**(10), 3208 (1995).
- S. Patankar, *Numerical Heat Transfer and Fluid Flow*, CRC Press (1980).
- W. J. Minkowycz, E. M. Sparrow, and J. Y. Murthy, *Handbook of Numerical Heat Transfer*, Wiley, John and Sons, Inc (2006).